Journal of Applied Fluid Mechanics, Vol. 18, No. 8, pp. 2053-2065, 2025.
Available online at www.jafmonline.net, ISSN 1735-3572, EISSN 1735-3645.
https://doi.org/10.47176/jafm.18.8.3313

Research on the Effects of Vane Geometry Parameters on Cyclone Pump Performance

J. Hong[1], Y. Jin[1], Z. Huang[1], W. Wang[1], Y. Gu[1†], C. Mou[2], D. Wu[1], Z. Wu, and J. Mou[1]

[1] *College of Metrology Measurement and Instrument, China Jiliang University, Hangzhou, 310018, China*
[2] *College of Energy Engineering, Zhejiang University, Hangzhou 310027, China*

†*Corresponding Author Email:* guyunqing@cjlu.edu.cn

ABSTRACT

The thickness, width, and outlet deflection angle of the cyclone pump vane are selected as research objects to enhance overall cyclone pump performance and minimize its energy loss. Numerical simulations of the flow field are conducted for five groups of impellers with different structures based on the realizable k–ε turbulence model. The analysis incorporates the velocity and pressure field distributions under various operating conditions to demonstrate how the primary geometrical parameters of the vane affect the cyclone pump's performance. The results show that although increasing the thickness of the vane can boost the pump's maximum efficiency within a limited range, excessive thickness narrows the flow channels between the vanes. This results in the pump reaching its lowest efficiency at a thickness of 4.4 mm. To prevent efficiency loss, the blade width should remain within a certain range. A slight increase in blade width improves the cyclone pump's flow stability, and its effect on the head is less than its impact on efficiency. Additionally, as the deflection angle at the vane's outlet increases, the low-pressure zone at the impeller's inlet slightly expands, and the pressure in the volute outlet flow passage slightly increases. These changes enhance flow stability and result in a more consistent pressure distribution in the volute pump's flow passage.

Article History

Received December 10, 2024
Revised January 18, 2025
Accepted March 23, 2025
Available online June 3, 2025

Keywords:

Cyclone pump
Numerical simulation
Vane thickness
Vane width
Vane outlet deflection angle

1. INTRODUCTION

Although cyclone pumps are widely used in various fields and are crucial for national fluid transportation, their efficiency is typically maintained at approximately 50% (Bordeasu et al., 2024). The energy loss resulting from the intricate flow field inside the pump is substantial (Wu et al., 2024). Various geometric parameters of the cyclone pump play a decisive role in its performance, making it essential to investigate how the pump's structure affects its performance behavior. Such studies aim to improve the pump's efficiency, reduce emissions and energy consumption, and increase head, among other objectives.

Regarding the impact of the cyclone pump's structure on its functionality and performance, key parameters include the outer diameter of the impeller, the width of the lobeless cavity, the number of vanes, the width of the vanes, and the form of the vanes (Fleder & Böhle, 2019; Gao et al., 2020; Chao et al., 2022; Xu et al., 2022). Among these, the impeller, as the primary overflow component, has a strong impact on the pump's head and efficiency (Zhao et al., 2023). Modifying its vane structure will alter the cyclone pump's internal flow field, which alters its performance (Yin et al., 2022) studied the effect of the length of the inclined section of the vane on the internal vortex structure and pressure distribution of the cyclone pump and found that a shorter inclined section improved the pump's anticavitation performance. Based on the bionic principle, a shark's gill slit jet structure was developed to stop cavitation in fluid machinery when flow conditions are high (Gu et al., 2023). Adding carbon nanotubes to new materials enhanced the tribological performance of fluid machinery surfaces (Gu et al., 2022). Five distinct types of centrifugal pumps with varying vane thicknesses were examined, and the optimal efficiency point of the pump shifted toward low-flow operating conditions and the pump efficiency increased marginally as the vane thickness increased within a specific range (Chen et al., 2015). The position and deflection angle of the diverter vane were examined in relation to the pump's pressure pulsation and radial force, the results showed that the diverter vanes could effectively prevent hydrodynamic vibration (Zeng et al., 2020). Existing studies on the effects of vanes on the internal flow of cyclone pumps found that increasing the number of vanes effectively

NOMENCLATURE

Q	flow rate	D_1	inlet diameter
H	head of the cyclone pump	D_2	outlet diameter
n	rotational speed	D	impeller diameter
P	power	φ	outlet deflection angle
Z	number of vanes	η	efficiency of the cyclone pump
b	vane width	P_1	pressure condition of the inlet boundary
e	vane thickness		

minimized the cavitation area at the vane inlets and resulted in a more uniform distribution of turbulent kinetic energy within the pump (Wang et al., 2023). The cyclone pump performance will fluctuate substantially when its working conditions change. Although there is plentiful research on the impeller's structural parameters, that research focuses on a single working condition under a single geometric parameter. Synchronization analysis of the research for multicondition, multiobjective structural parameters is still comparatively rare.

Therefore, to investigate the influence of blade geometric parameters on the internal flow field and performance of cyclone pumps, numerical simulations using the realizable k–ε turbulence model are used to study the influence of each blade form on the pressure, velocity, and vortex distribution in the internal flow field under different flow rates from the three aspects of blade thickness, width, and outlet deflection angle. These investigations provide new ideas and comprehensive reference bases for the optimization of cyclone pump vanes and the search for the best pump working conditions.

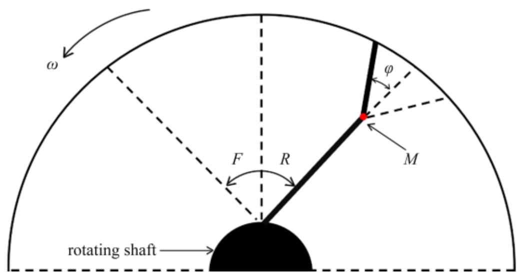

(a) Bi-directional inclined blade structure form

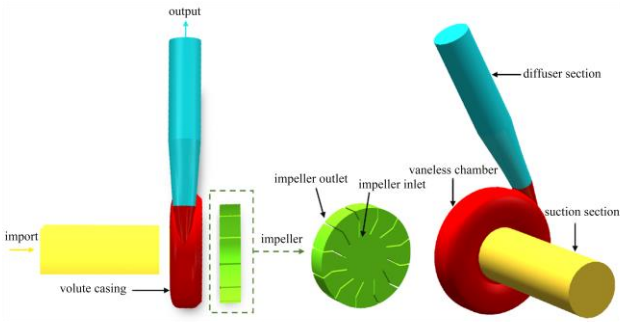

(b) Integral (c) Impeller fluid domain (d) Worm gear fluid domain

Fig. 1 Cyclone pump model

2. STRUCTURAL MODELING AND NUMERICAL SIMULATION METHODS

2.1 Geometric Modeling

An IS150-100-300 model cyclone pump is selected for this study. Its standard performance parameters are as follows: flow rate Q/Q_d = 216 m^3/h, head H = 150 m, rotational speed n = 2980 r/min, power P = 315 kW, number of vanes Z = 12, vane width b = 65 mm, thickness of vane e = 4 mm, inlet diameter D_1 = 150 mm, outlet diameter D_2 = 100 mm, and impeller diameter D = 300 mm. The impeller structure is shown in Fig. 1(a). The impeller uses bidirectional tilting inclined blades (R30-F30). The oblique angle of the second inclined section of the blade is the outlet deflection angle φ; changes in the size of φ change the blade outlet angle.

The computational domain of the cyclone pump model consists of four parts: the impeller inlet section, the impeller, the worm casing, and the impeller outlet section. Three-dimensional (3D) modeling of the cyclone pump parts is conducted using 3D software to extract the computational domain of the internal pump flow. The fluid domain model is shown in Fig. 1.

2.2 Turbulence Model Selection

Numerical simulation techniques are used to conduct research on the internal flow mechanisms of fluid machinery (Liu et al., 2021; Li, 2022; Zhang et al., 2024).

A customized density function has been used to calibrate various turbulence models to increase the simulation accuracy of nonconstant hydrofoil cavitation (Gu et al., 2024). Current research has numerically simulated a hydrofoil using an improved k–ω turbulence model, demonstrating that the high degree of coupling between chord position and the microwedge structure inhibits cavitation (Qiu et al., 2024).

Among the diverse types of turbulence models, the realizable k–ε model is a high-Reynolds-number turbulence model that effectively manages complex secondary flows, boundary layer flows with strong backpressure gradients, and rotating flows by considering the impact of the mean spin in determining the turbulence viscosity. It is suitable for a wide range of flows because it corrects the turbulent viscosity, especially in simulations involving complex flow characteristics, and it can simulate moderately complex flows such as jets, separating flows, secondary flows, and rotating flows, in addition to simulating circular jets with high simulation accuracy. In the assessment of the standard k–ε, Re-Normalization Group (RNG) k–ε, and realizable k–ε models for describing the turbulent flow field of a pump impeller, the Multiple Reference Frame (MRF) and Sliding Mesh (SM) approaches were employed. Although

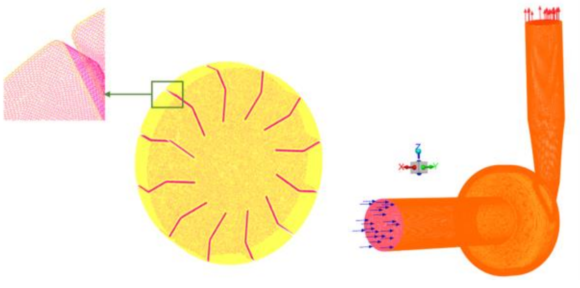

(a) Impeller fluid domain meshing (b) Worm shell fluid domain meshing

Fig. 2 Fluid domain meshing

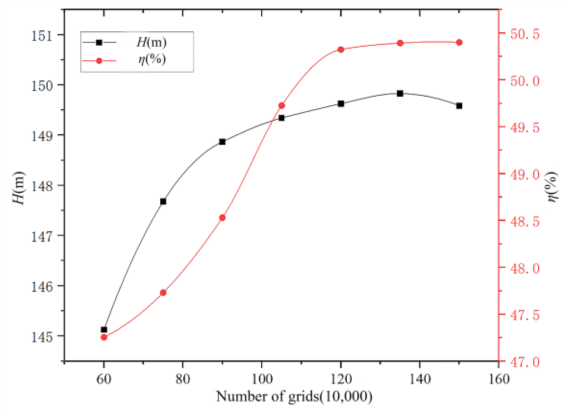

Fig. 3 Results of the effect of the number of grids on the numerical simulation

the RNG k–ε model enhances predictions of turbulent kinetic energy and dissipation rate, the realizable k–ε model demonstrates superior performance across the MRF and SM methodologies (Mendoza-Escamilla et al., 2018). The realizable k–ε model is chosen over the standard k–ε model and the RNG k–ε model due to its superior accuracy, convergence, and capacity to manage complex issues.

2.3 Basin-Wide Meshing and Boundary Condition Setting

Meshing is crucial for the accuracy of numerical simulations. Hexahedral meshing provides superior uniformity and continuity compared to tetrahedral meshing, and it is particularly well-suited for managing complex geometries and boundary conditions. Therefore, the hexahedral mesh is selected for high-precision discretization of the main pump computational domain. Hexahedral meshes of the impeller and the worm shell, which are the primary objects of this study, have been encrypted to ensure that their quality satisfies the simulation requirements. The overall computational mesh model is presented in Fig. 2. During mesh generation, topology optimization and node distribution adjustments were conducted based on the geometric characteristics of each region, to ensure mesh quality and computational domain resolution. The size and scale factor of the global mesh should be chosen carefully to ensure mesh adaptability. In this work, the mesh quality of each model is strictly controlled to ensure that the minimum mesh quality is more than 0.5, which improves the reliability and accuracy of the calculation.

The simulation boundary conditions are as follows: the inlet is Mass-flow-inlet, and the outlet condition is set as Pressure-outlet; the rotational speed n = 2980 r/min; the mass flow rate of the inlet boundary condition is set as 60 kg/s, and the pressure condition of the inlet boundary is set as P_1 = 101325 Pa. The near-wall region is treated using the standard wall-function method and the SIMPLE algorithm is used to solve the velocity and pressure coupling problem. A multiple reference coordinate system is used in which the impeller is the rotor, the other components are the stator, and the interface between the impeller and the lobeless cavity is set as the interface to realize the data interactions between the computational domains of each component. The turbulence intensity is medium (intensity = 5%). All the wall surfaces are set to be no slip. In terms of solving control, the maximum iteration step is set to 10,000 to ensure the stability and convergence of the computational process and the residual objective in the residual convergence criterion is set to 10^{-6}. Convergence is calculated when all the monitored values have reached a stable state.

Performance simulations are conducted at 0.6 times the design flow rate ($0.6Q_d$), 0.8 times the design flow rate ($0.8Q_d$), full load design flow rate ($1.0Q_d$), 1.2 times the design flow rate ($1.2Q_d$), and 1.4 times the design flow rate ($1.4Q_d$) to investigate the effects of key vane geometric parameters on cyclone pump performance characteristics. Vane width (e), vane thickness (b), and outlet deflection angle (φ) each had five values for the simulation, as follows: e = 3.2 mm, 3.6 mm, 4.0 mm, 4.4 mm, and 4.8 mm; b = 52 mm, 58.5 mm, 65.0 mm, 71.5 mm, 75.0 mm; and φ = 24°, 27°, 30°, 33°, and 36° are selected for simulation. Detailed simulation calculations were conducted one by one under each of the five different working conditions to investigate the mechanisms of influence on cyclone pump performance (head and efficiency).

2.4 Mesh-independence Verification and Accuracy of Numerical Simulations

Mesh-independence verification is conducted to analyze the calculation results under different mesh densities, identifying the range of mesh numbers where the calculation results change less or tend to be stable. This helps determine the appropriate number of meshes. Head and efficiency are the two primary characteristic parameters of a cyclone pump. Head represents the height to which the cyclone pump can elevate liquid, effectively indicating the increase in energy per unit weight of liquid as it passes through the pump. Efficiency is defined as the ratio of effective power to shaft power, indicating the extent of energy loss during pump operation. Therefore, in this work, the head (H) and efficiency (η) of the cyclone pump are selected as the parameters for checking the mesh independence. The test results are shown in Fig. 3. When the number of meshes of the model pump is greater than 1.2 million, the head and efficiency of the cyclone pump stabilize, and the error is less than 2%. Considering the requirements of calculation accuracy and calculation

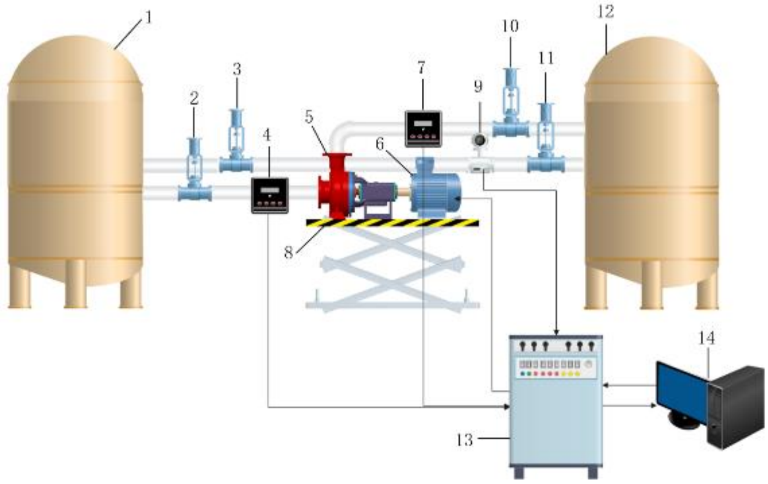

1. water storage tank; 2. water storage tank inlet valve; 3. water storage tank outlet valve; 4. inlet manometer; 5. experimental pumps; 6. motors; 7. export press; 8. lifting table; 9. electromagnetic flowmeter; 10. stabilizer tank inlet valve; 11. stabilizer tank outlet valve; 12. stabilizer tank; 13. electronic control cabinet; 14. upper computer

Fig. 4 Schematic diagram of the experimental setup for the external characteristics of cyclone pumps

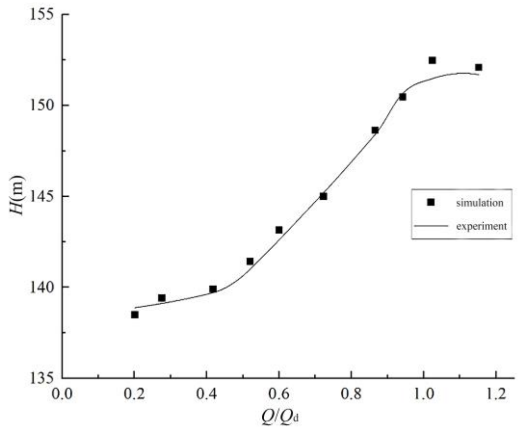

(a) Head-flow curves

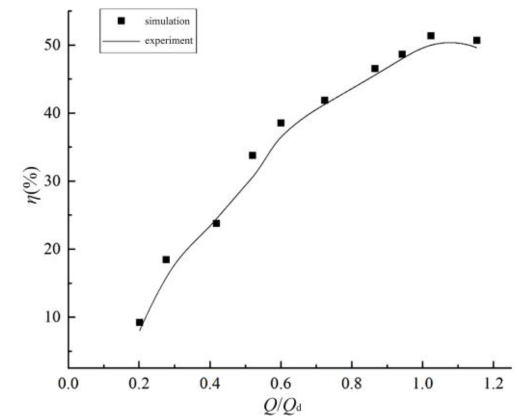

(b) Efficiency-flow curves

Fig. 5 Plot of experimental and simulated characteristics

efficiency, the total number of calculation meshes of the model pump is finally set as 1,286,545, which not only ensures the accuracy of the calculation results and can fully describe the flow field's characteristics, but also calculates quickly and efficiently and increases work efficiency.

To confirm the viability of the computational model, a cyclone pump external characteristic experiment was conducted to measure the cyclone pump's actual hydraulic performance. The IS150-100-300 cyclone pump was used in the experiment. The experimental conditions aligned with the numerical simulation conditions. Figure 4 shows the schematic of the external characterization test setup.

The experimentally measured data of the cyclone pump initial operating state were analyzed against the numerical simulation output obtained based on the preliminary model to ensure the validity and reliability of the numerical simulation. The efficiency and head values were compared, and the results are shown in Fig. 5.

Appropriate simplifications and assumptions about the pump structure are unavoidably made during the numerical modeling process of pump fluid flow. The mechanical losses, friction losses, and motor efficiency losses of actual experiments mean that the simulation and experimental efficiency results are bound to have a certain error between the results. Calculated, the average error in efficiency and head is less than 3%. Comprehensive analyses of the external characteristics under different flow rates can be used to determine that the early-stage cyclone pump modeling and simulation techniques were reasonable and realistic, allowing them to be applied to further research.

3. EFFECT OF DIFFERENT VANE THICKNESSES ON CYCLONE PUMP PERFORMANCE

Figure 6 illustrates how various vane thicknesses perform differently under the various operating conditions mentioned in Section 2.3. Figure 6(a) shows the effect of the five vane thicknesses on the cyclone pump head under different flow rates. Despite the complexity of the internal flow, from an overall perspective, the head of the cyclone pump model with varying vane thicknesses increases and then decreases as the flow rate increases. In the 1.0 Q_d case, the increase in vane thickness narrows the adjacent vane spacing, which in turn leads to a narrowing of the flow channel space restriction. When the fluid is discharged outward through the impeller, it expands

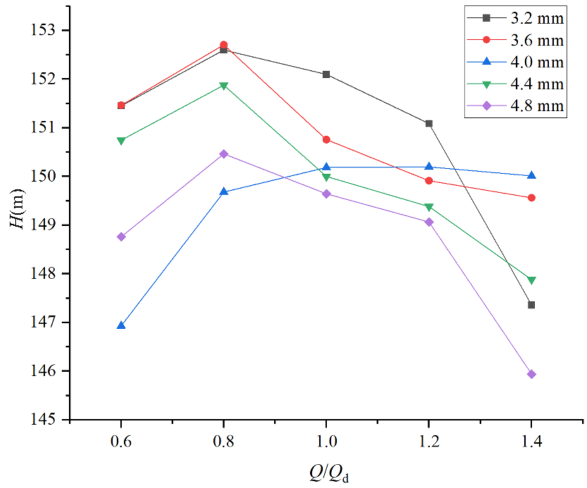

(a) Influence of blade thickness on head

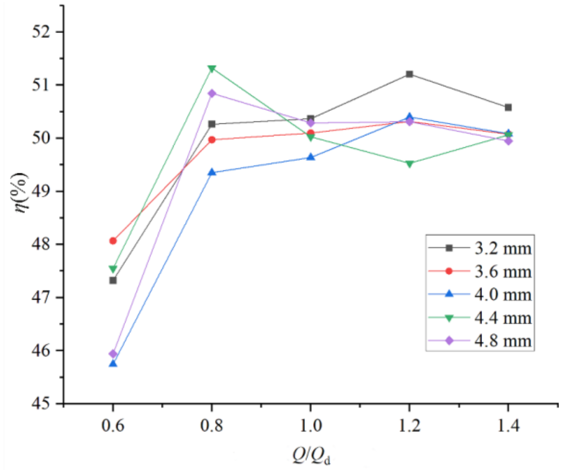

(b) Effect of blade thickness on efficiency

Fig. 6 Impact of varying vane thicknesses on cyclone pump performance under various operating circumstances

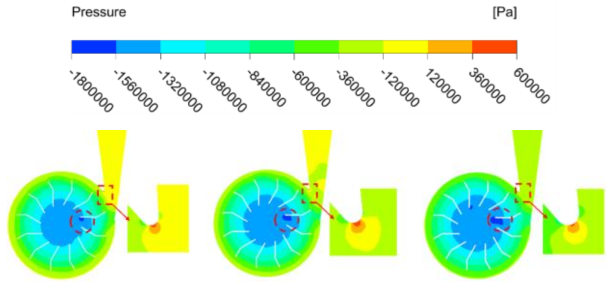

(a) e=3.2 mm (b) e=3.6 mm (c) e=4.0 mm

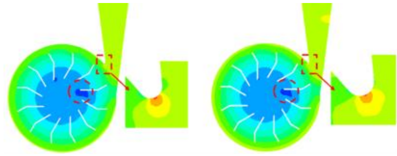

(d) e=4.4 mm (e) e=4.8 mm

Fig. 7 Cross section of pressure distribution at 0.8Q_d

rapidly, and this rapid expansion of the flow velocity forms a vortex in the outlet region of the impeller.

Figure 6(b) illustrates how the cyclone pump efficiency is affected by varying vane thicknesses under five different flow rates. The efficiency of the cyclone pump shows a flat trend with increasing vane thickness compared to the variations in the head. When the flow rate increased from 0.6 Q_d to 0.8 Q_d, the efficiency of each group increases, and the most obvious change in efficiency is observed for vane thicknesses e = 4.0 mm and e = 4.8 mm, with increases of 3.60% and 4.90%, respectively. The efficiency of the pump with vane thicknesses of e = 4.4 mm and e = 4.8 mm drops dramatically when the flow rate increases to the rated condition of 1.0 Q_d, with the latter dropping by 0.64%. As the flow rate increases, the efficiencies of the other blade thicknesses slightly increase. At the working condition of 1.2 Q_d, the efficiency decreases gradually as the blade thickness increases from 3.2 mm to 4.4 mm, reaching the lowest efficiency at 4.4 mm.

3.1 Pressure Distribution Analysis for Different Vane Thicknesses

The pressure and velocity fields of the cyclone pump's internal flow have been analyzed to fully investigate the impact of the vane's initial geometric parameters on pump performance, considering the complex features of the internal flow field. Two representative working conditions of low flow rate and high-flow rate, which are 0.8 Q_d and 1.2 Q_d, were chosen from the simulated conditions based on the performance curves. Figures 7 and 8 show the cross sections of cyclone pump pressure field distributions with different vane thicknesses at 0.8 Q_d and 1.2 Q_d.

As illustrated in Figs. 7 and 8, the nonuniform pressure distribution within the cyclone pump model is attributable to the asymmetric structure of the volute shell. This structural characteristic results in a pronounced imbalance in the internal flow field pressure distribution. In this segment of the work, although the vane thickness varies across the cyclone pump model, the pressure distribution trend remains consistent in the cross-sectional fluid domain. In Figs. 7 and 8, as the fluid flows through the impeller outlet into the worm casing, there is an obvious change to high pressure near the spacer tongue. The highest pressure of the whole pressure cross-section distribution map is near the spacer tongue. As fluid flows through the tongue into the worm shell outlet, the pressure gradually decreases. Like Fig. 7 (0.8 Q_d), the red circular outline in Fig. 8 indicates a distinct localized low-pressure area in the impeller outlet under the same operating conditions. With the increase of blade thickness, the shape of the low-pressure area in the impeller did not change noticeably, but the area of low-pressure area gradually increased. When the blade thickness increased from e = 3.2 mm to e = 3.8 mm, the phenomenon of localized low pressure occurs in the worm shell outlet runner. When e increases to 4.0 mm, the localized low pressure decreases, and the pressure of the entire worm shell outlet runner uniformly decreases. The pump's interface pressure and

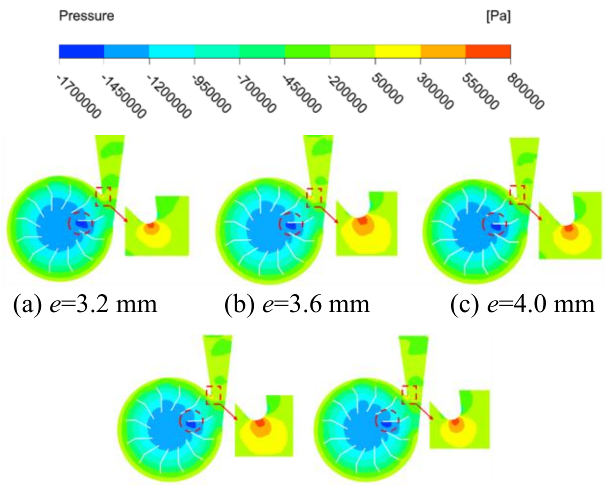

(a) e=3.2 mm (b) e=3.6 mm (c) e=4.0 mm

(d) e=4.4 mm (e) e=4.8 mm

Fig. 8 Cross section of pressure distribution at 1.2*Q*d

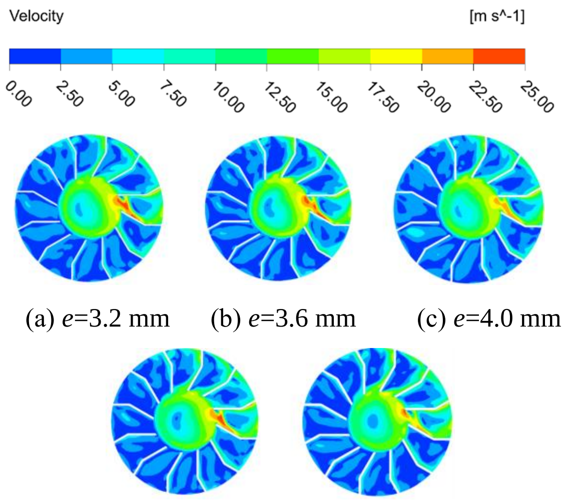

(a) e=3.2 mm (b) e=3.6 mm (c) e=4.0 mm

(d) e=4.4 mm (e) e=4.8 mm

Fig. 9 Vector plot of cyclone pump speed at 0.8*Q*d

pressure gradient drop with increasing thickness. The worm shell outlet pipe experiences a significant drop in pressure.

We also compared the pressure distribution of the same vane thickness under different working conditions, as shown in Fig. 7(c) and Fig. 8(c). The pressure distribution gradient in the pump is larger under high-flow conditions, and the distribution in the worm casing outlet runner is quite turbulent. One of the reasons for the reduced head of the cyclone pump at 1.2 Q_d is the instability of the flow field compared to lower flow rates.

3.2 Velocity Field Analysis for Different Vane Thicknesses

The velocity distributions in the internal flow field of the cyclone pump model with five blade thicknesses at 0.8 Q_d and 1.2 Q_d flow rates are shown in Figs. 9 and 10. When the fluid enters the impeller, the flow stabilizes in the pump inlet flow channel toward a lower velocity, while the velocity increases significantly in the impeller's outlet region, reaching a peak value. In the impeller channel, due to the accelerating effect of blade rotation on the fluid, the velocity of the fluid at the leading edge of the blade is higher than that at the trailing edge part of the blade.

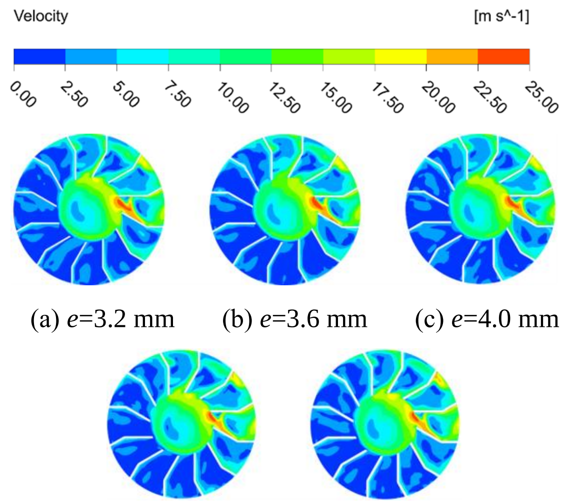

(a) e=3.2 mm (b) e=3.6 mm (c) e=4.0 mm

(d) e=4.4 mm (e) e=4.8 mm

Fig.10 Vector plot of speed of cyclone pump under 1.2*Q*d

Figure 9 shows that the velocity distribution change trend in the pump is consistent across the different blade thicknesses. The velocity gradient decreases as e increases, and the low velocity region in the velocity cloud map increases accordingly, but the impeller outlet region still maintains the highest velocity. As can be observed, the speed near the spacer tongue increases substantially. Specifically, the velocity at the outlet wall near the tongue is higher compared to that of the wall away from the tongue. As the fluid moves through the outlet, severe backflow occurs due to the higher speed, resulting in lower efficiency. Under high-flow rates, the relative velocities of the five models with different blade thicknesses shown in Fig. 10 are all higher than those under the 0.8 Q_d flow rate.

3.3 Velocity Streamline Distribution for Different Vane Thicknesses

As illustrated in Figs. 11 and 12, the low flow rate condition, represented by 0.8 Q_d, and the high-flow rate condition, represented by 1.2 Q_d, are again chosen to analyze the velocity distribution in the cyclone pump and more intuitively compare and analyze the velocity field inside the pump. Figure 11 shows that each model interface has varying degrees of vortex-based flow lines. Figure 11(d) shows that the vortex takes up most of the impeller channel and that the flow is more turbulent. The velocity streamline distribution pattern exhibits a relatively higher degree of similarity overall. Vortices emerge in the vicinity of the blade outlet. This phenomenon can be attributed to the fact that, at the intersection of the impeller and the volute casing, the volute casing remains stationary, whereas the impeller must rotate. The static–dynamic interaction between the impeller and the volute casing leads to a more frequent occurrence of vortices. When the fluid exits the impeller

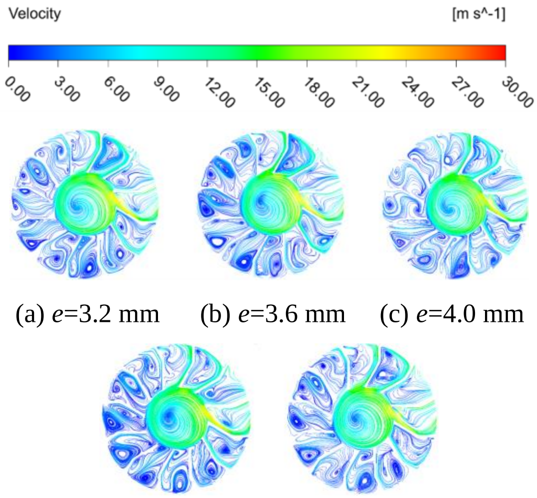

(a) e=3.2 mm (b) e=3.6 mm (c) e=4.0 mm

(d) e=4.4 mm (e) e=4.8 mm

Fig. 11 Impeller velocity streamlines at 0.8Q_d

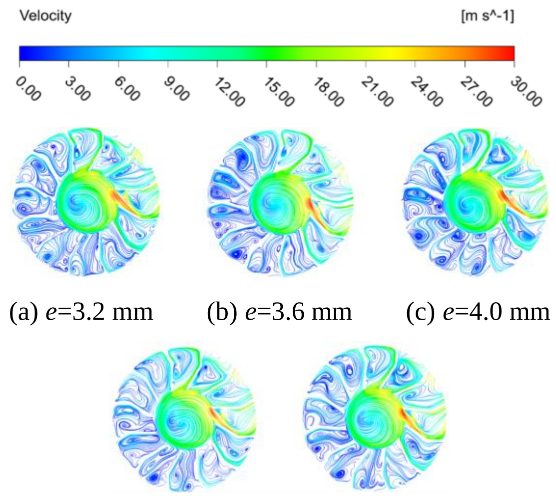

(a) e=3.2 mm (b) e=3.6 mm (c) e=4.0 mm

(d) e=4.4 mm (e) e=4.8 mm

Fig. 12 Impeller velocity streamlines at 0.8Q_d

channel, some of it will infiltrate another impeller channel, thereby inducing secondary flow, which is one cause of vortex generation.

At the same operating conditions, when e increases from 3.2 mm to 4.0 mm, the relative velocity within the pump reduces substantially and, simultaneously, the number of vortices in the flow field decreases. Near the impeller outlet and the worm casing, the velocity streamlines are relatively more regular and the number of vortices is minimized. When e increases to 4.4 mm, the relative velocity in the pump increases, and the number of vortices also increases substantially. There is an obvious localized low-speed region at the impeller inlet, but the flow line near the worm casing is more regular compared to that at e = 3.2 mm.

Comparing the velocity streamline distributions under two different flow rates, as illustrated in Fig. 11 and 12, it is evident that the number of vortices within the velocity field increases significantly under high flow rate conditions, resulting in more turbulent streamlines. Observation of the direction of the streamlines shows that more fluid enters another impeller channel after the outflow, and the streamlines in the second channel are more complicated, destabilizing the flow field. Comparing Fig. 11(b) with Fig. 12(b), it can be observed that when the cyclone pump is operated at a high-flow rate, the flow lines at the worm casing become intricate, which substantially increases the number of generated vortices. Part of the fluid will be impeded, or reverse flow will occur due to momentum exchange, exacerbating the backflow phenomenon and, consequently, increasing energy losses. This situation not only increases wear within the pump but also adversely affects its overall efficiency.

4. EFFECT OF DIFFERENT VANE WIDTHS ON CYCLONE PUMP PERFORMANCE

Different vane widths will change the amount of fluid entering the lobeless cavity during pump operation. This variation has a direct impact on the stability of the pump and will further affect its overall operating efficiency. The effects of different vane widths on the head and efficiency of the cyclone pump are shown in Fig. 13(a) and 13(b).

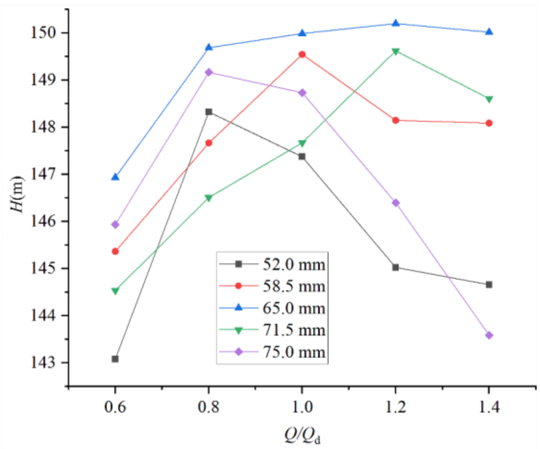

(a) Effect of blade width on head

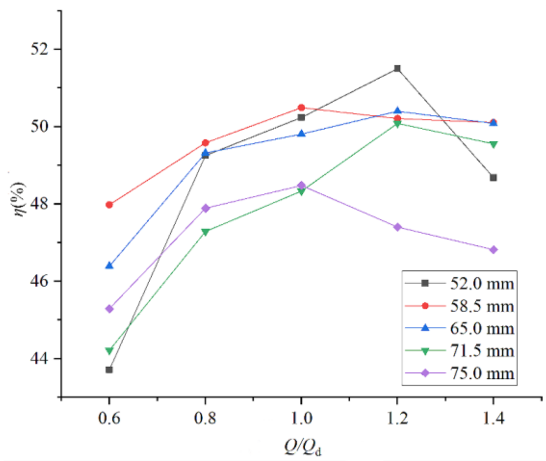

(b) Effect of blade width on efficiency

Fig. 13 Effect of different vane widths on cyclone pump performance

Figure 13(b) shows the cyclone pump efficiency trend variation with flow rate for different impeller widths. The efficiency variation patterns of cyclone pumps designed with different vane widths show some similarity: as the flow rate increases, the efficiency may improve. Under the 0.6 Q_d flow rate, the efficiencies of the five blade width models are low. As the flow rate increases to 0.8 Q_d and then to 1.0 Q_d, the efficiencies of the cyclone pumps under each blade width configuration increase substantially. With the increase of b, the high efficiency zone of the cyclone pump shifts to the high-flow rate. The efficiency for b = 52.0 mm has the largest increase, of approximately 6%. The efficiency for b = 65.0 mm is 51.8% at 0.8 Q_d, which is 4.5% higher than that of 0.6 Q_d. At 1.0 Q_d, the best performance is achieved. When the impeller width is reduced to 58.5 mm and 52.0 mm, the efficiency decreases. The efficiency of b = 58.5 mm is 50.5%, and the efficiency of b = 52.0 mm is 50.2%. The efficiency performance of all five widths decreases at 1.2 Q_d. As the impeller vane width increases, the volume of the lobeless cavity in front of the impeller is reduced. When the fluid enters the lobeless cavity, the circulation flow area narrows. The vanes break down the large vortices into small vortices, thus improving the stability of the fluid flow. However, larger b values make the cyclone pump operation more variable. When b grows to a specific threshold, the efficiency of the cyclone pump will not continue to increase but will instead decline. Therefore, the overall efficiencies of b = 71.5 mm and b = 75.0 mm are poor compared to the other impeller widths, and it can be concluded that an appropriate increase in vane width is favorable for obtaining better hydraulic performance of the cyclone pump.

4.1 Pressure Field Analysis for Different Vane Widths

As in Section 3, the flow calculation results at two representative flow rates of 0.8 Q_d and 1.2 Q_d were selected and analyzed. Figures 14 and 15 show cross sections of the pressure distributions at the two flow rates. Observing Figs. 14 and 15, the pressures of the five basic models with different vane widths are gradually increasing from the inlet to the outlet direction at all flow rates. Overall, the pressure around the worm casing is markedly higher than that in the flow channel area of the impeller, and the pressure at the outlet pipe is slightly higher under the high-flow condition than under the low flow condition. Under the high-flow condition, the highest pressure value does not appear in the outlet pipe but is shifted to the flow channel area near the impeller outlet. The highest pressure is substantially higher than that found in the outlet pipe area under the low flow rate. At the impeller inlet, the fluid is at a lower pressure and when it enters the impeller, the pressure gradient is larger. The pressure at the suction surface of the vane is negative, and due to the high rotational speed of the fluid when it goes around the head of the vane, this is where cavitation is most likely to occur.

Figure 14 shows that localized low pressure develops in the low-pressure region at the impeller inlet as the blade width increases. At b = 58.5 mm, the localized low-pressure area is the largest, and it gradually decreases when b > 58.5 mm. Simultaneously, the high-pressure area at the spacer tongue grows as the blade width increases.

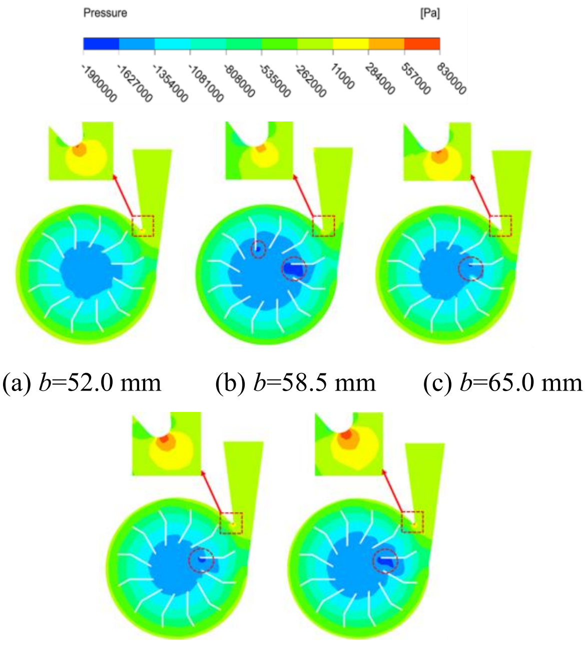

(a) b=52.0 mm (b) b=58.5 mm (c) b=65.0 mm

(d) b=71.5 mm (e) b=75.0 mm

Fig. 14 Cross section of pressure distribution at 0.8Q_d

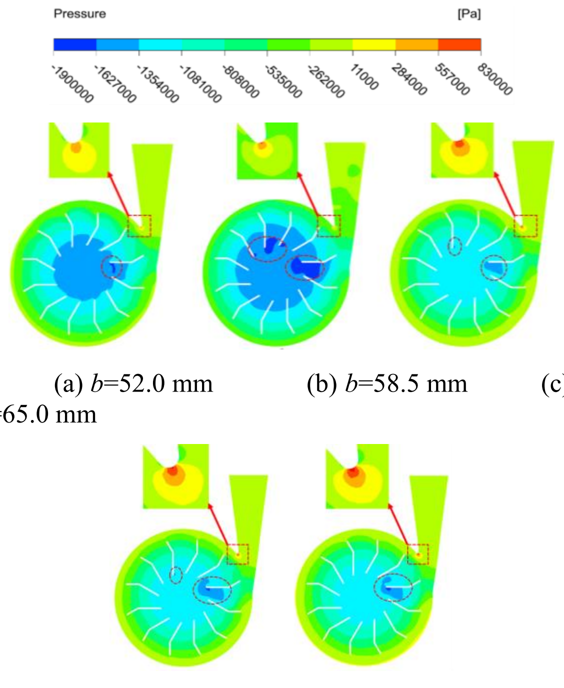

(a) b=52.0 mm (b) b=58.5 mm (c) b=65.0 mm

(d) b=71.5 mm (e) b=75.0 mm

Fig. 15 Cross section of pressure distribution at 1.2Q_d

This is because the wider blade reduces the fluid-winding in the impeller during operation, which reduces energy loss and improves the efficiency of converting rotational energy into pressure energy.

When the flow rate increases, the pressure gradient inside the cyclone pump increases substantially. The diffusion of the localized low-pressure region in the impeller inlet in Fig. 15(b) is obvious, and the pressure distribution is not uniform in the worm casing outlet pipe. Stability has been impacted, and the impeller's localized pressure field changes substantially when b rises to 65.0 mm. This can result in flow separation, vortices, and other complex flow phenomena. However, when $b > 58.5$ mm, the localized low-pressure area gradually decreases. This change is consistent with the change in Fig. 14 at the 0.8 Q_d condition. Observation of Fig. 15 shows that the area of the spacer tongue of the high-pressure area greatly increases compared to that under the 0.8 Q_d flow rate. In the high-flow condition, the fluid flow rate through the impeller outlet into the worm casing increases and its impact becomes stronger. The pressure in the worm casing spacer tongue is noticeably higher than that in the low-flow conditions.

4.2 Velocity Field Analysis for Different Vane Widths

The cross-sectional velocity vector distributions in the pump corresponding to different impeller widths for the 0.8 Q_d and 1.2 Q_d flow rates are shown in Figs. 16 and 17. Comparing the two figures, there are obvious inhomogeneities in the velocity distributions inside the cyclone pump, especially in the impeller channel and the worm casing outlet pipe, where the fluid velocity is relatively lower. Whereas three of the impeller channels have substantially higher internal velocities close to the spacer tongue, the distribution of velocity vectors within the remaining impeller channels shows a degree of uniformity. This phenomenon is particularly noticeable near the roots of the impeller vanes, due to the low absolute velocity of the fluid in these regions. As the impeller continues to rotate, the absolute velocity of the fluid increases near the front of the vane. Such a velocity distribution reveals the complexity of the hydrodynamic behavior inside the impeller.

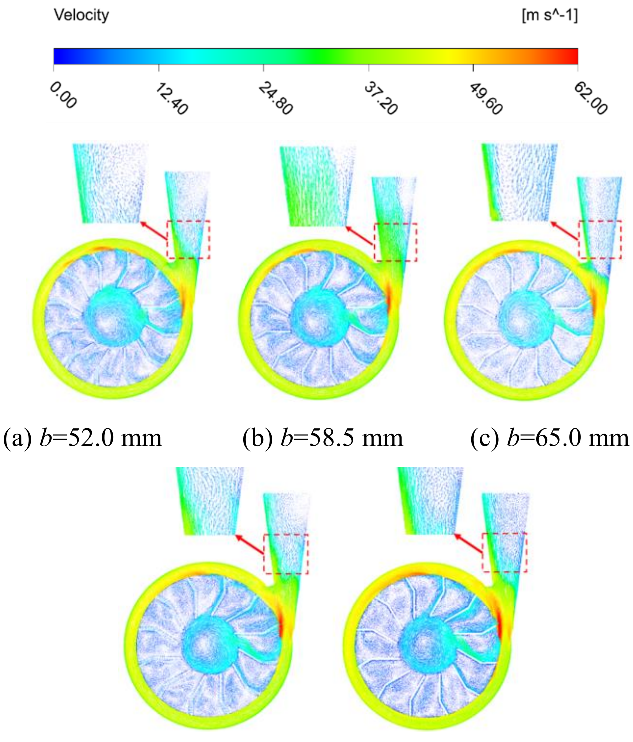

(a) b=52.0 mm (b) b=58.5 mm (c) b=65.0 mm

(d) b=71.5 mm (e) b=75.0 mm

Fig. 16 Velocity vector diagram at 0.8Q_d

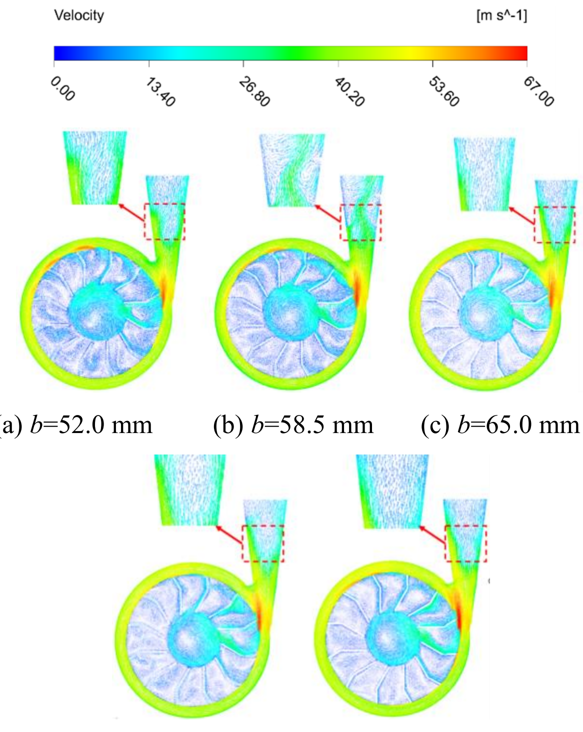

(a) b=52.0 mm (b) b=58.5 mm (c) b=65.0 mm

(d) b=71.5 mm (e) b=75.0 mm

Fig. 17 Velocity vector diagram at 1.2Q_d

It is evident from the local enlargement in Fig. 16(a) that the outlet flow channel exhibits backflow at b = 52.0 mm. This is because the fluid's velocity decreases as it enters the worm shell due to the worm shell's diffusion structure, and the impeller's velocity field will fluctuate close to the spacer tongue. This phenomenon will improve as the vane width increases. At b = 58.5 mm, the velocity in the worm shell outlet flow channel is higher, and the velocity distribution is more uniform. From Fig. 16, it can be observed that the number of vector arrows inside the impeller decreases during the continuous increase from b = 52.0 mm to b = 65.0 mm, and thus the width of the vanes affects the fluid velocity distribution in the impeller. A wider vane creates a larger obstruction zone at its front end, which changes the velocity gradient of the inflowing fluid. Simultaneously, wider vanes promote the formation of more compact vortices at their front ends. These vortices help to stabilize the fluid velocity field, but they also can cause localized flow velocities to be too high. It can be observed from Figs. 16(d), 16(e), 17(d), and 17(e) that the velocities of localized high-velocity zones in the impeller outlet near the spacer tongue are greatly increased, which in turn affects the efficiency and stability of the pump.

5. INFLUENCE OF VANE OUTLET DEFLECTION ANGLE ON CYCLONE PUMP PERFORMANCE

Figure 18 displays the hydraulic performance trends of various vane outlet deflection angles under five distinct operating conditions. The cyclone pump head change trend in Fig. 18(a) shows that when the flow rate increases, the head increases and then decreases. At a low flow rate of 0.6 Q_d, the head peaks at φ = 33°, and the head is lowest

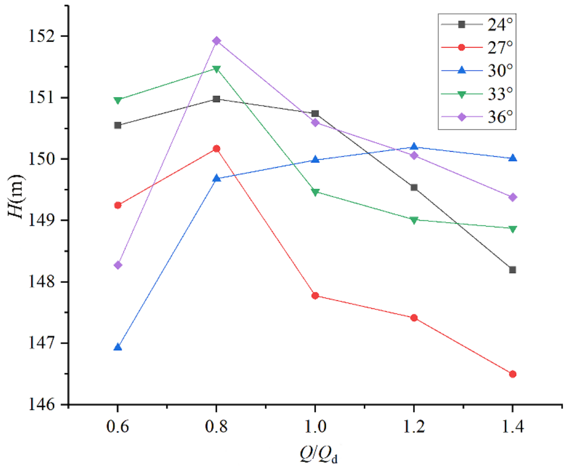

(a) Influence of blade outlet deflection angle on head

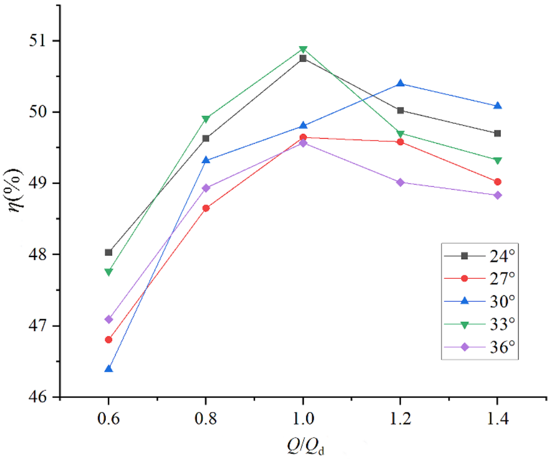

(b) Effect of blade exit deflection angle on efficiency

Fig. 18 Effect of different vane outlet deflection angles on cyclone pump performance

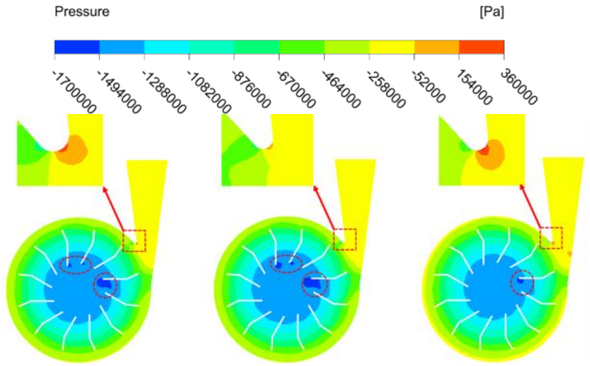

(a) φ=24° (b) φ=27° (c) φ=30°

(d) φ=33° (e) φ=36°

Fig. 19 Pressure distribution cross section at 0.6*Q*d

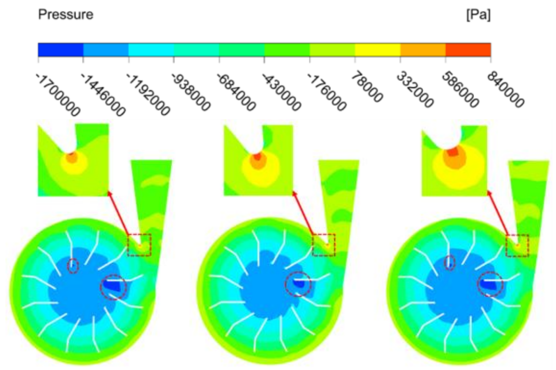

(a) φ=24° (b) φ=27° (c) φ=30°

(d) φ=33° (e) φ=36°

Fig. 20 Pressure distribution cross section at 1.0*Q*d

when φ = 30°. When the flow rate increases from 0.6 Q_d to 0.8 Q_d, the head performances of the five different outlet deflection angles of 24°, 27°, 30°, 33°, and 36° increase by 1.3%, 1.1%, 2.2%, 0.2%, and 2.4%, respectively. The growth trends of φ = 30° and φ = 36° are similar. φ = 27° and φ = 33° have similar overall trends, and their highest head values appear under the 0.8 Q_d flow rate. When the flow rate increases to 1.4 Q_d, the head performance of the five blade outlet angles decreases compared with the low flow rate.

Figure 18(b) shows the obvious and consistent effect of changing the outlet deflection angle, φ, on the cyclone pump efficiency. The figure shows that the highest relative efficiency is found near the rated working condition of 1.0 Q_d for φ = 24°, φ = 27°, φ = 33°, and φ = 36°. Additionally, at 1.2 Q_d, φ = 30° reaches its maximum efficiency of 50.40%. The efficiency of various angles is greatly improved and the growth trend is the same when the flow rate increases from 0.6 Q_d to 1.0 Q_d. In contrast, the efficiency at the 0.6 Q_d flow rate is low. Compared to the other four angles, the efficiency at φ = 30° is higher at 0.8 Q_d and 1.0 Q_d. Efficiency falls as the flow rate increases to 1.2 Q_d. The region of high efficiency shows up at 1.0 Q_d.

5.1 Pressure Field Analysis for Different Vane Exit Deflection Angles

The cyclone pump performance fluctuates substantially when the flow rate increases from 0.6 Q_d to 1.0 Q_d. Therefore, the two conditions of 0.6 Q_d and 1.0 Q_d are chosen to investigate the effects of outlet deflection angle on the cyclone pump hydraulic performance and the internal flow field. Figures 19 and 20 show the pressure distribution cross sections for different outlet deflection angles under 0.6 Q_d and 1.0 Q_d flow rates, respectively. From the figure, it is evident that the pressure distribution exhibits consistent features when the outlet deflection angle varies. In the impeller inlet, fluid pressure is low and the pressure gradient is high. When the fluid rotates too quickly around the head of the vane, the pressure will increase. With the rapid movement of the fluid to the outlet, the outlet pressure also increases.

From Fig. 19, it can be seen that with the increase of φ, the low-pressure region at the impeller inlet slightly enlarges. The change is not obvious when φ = 30°. The trends of pressure distribution at the five impeller outlet deflection angles in the figure are the same, with little change in the pressure gradient; whereas, the localized low-pressure and high-pressure regions at the impeller inlet and the worm shell are quite different. In Fig. 19(b) and 19(d), the localized low-pressure areas are larger, and the high-pressure areas at the spacer tongue are smaller compared with the other three cases. As shown in Fig. 19(c), when φ = 30°, two high-pressure areas occur in the pressure field at the impeller outlet and near the spacer tongue, however, the localized low-pressure area at the impeller inlet is substantially reduced. Comparing Figs. 19 and 20, the shape of the low-pressure region at the impeller inlet becomes irregular and turbulent under the high-flow condition, and the localized low-pressure area in the flow channel near the impeller outlet increases compared with the low-flow condition. Comparing Fig. 20(a) and 20(c), the pressure in the worm shell outlet runner will slightly increase with the increase of φ, and the pressure distribution will be more uniform.

5.2 Velocity Distribution for Different Vane Exit Deflection Angles

Figure 21 displays the cross section of the velocity distribution in the pump with various outlet deflection angles under the operating condition of 0.6 Q_d. When the outlet deflection angle changes, the velocity distribution is not uniform, but the velocity field distribution inside the cyclone pump is still consistent. The suction side of the vane has a lower velocity than the pressure side, and the velocity changes from the impeller inlet to the impeller outlet ranges from low to high. There is a localized region of low velocity in the impeller inlet. A sizable high-velocity region is produced in the blade duct near the worm casing outlet and spacer tongue, particularly in the blade flow paths along the rotational direction and near the spacer tongue, where the high-velocity flow dominates the blade's outlet region. As the outlet deflection angle φ increases, the overall velocity increases, and the local low-velocity zone shrinks. Increasing φ will widen the flow channel, which, in turn, decreases the blade's ability to move the fluid, resulting in hydraulic power loss.

The cross section of velocity distribution in the pump with different outlet deflection angles at 1.0 Q_d is shown in Fig. 22. The trend of the velocity field at 1.0 Q_d is consistent with that of 0.6 Q_d. The overall low-speed area becomes larger, and the velocity gradient obviously changes. In Fig. 22, when the outlet deflection angle increases from φ = 24° to φ = 30°, the velocity in the high-speed region of the impeller outlet decreases slightly. When φ increases 36°, the velocity in the high-speed region increases suddenly, indicating the existence of nonlinear effects. The head, efficiency, and other performance aspects of a cyclone pump are mutually constrained. An increase in the pump head may reduce the efficiency, making it impossible for the head and efficiency to reach their maximum values simultaneously. Complex, and often nonlinear, relationships exist between the geometric parameters of a cyclone pump and its performance. The slightest alteration in the geometric parameters of a cyclone pump can cause substantial fluctuations in its performance. Compared with the low-flow condition in Fig. 21, the velocity distribution in the impeller channel at this moment is not uniform, and the gradient change is more obvious in Fig. 22.

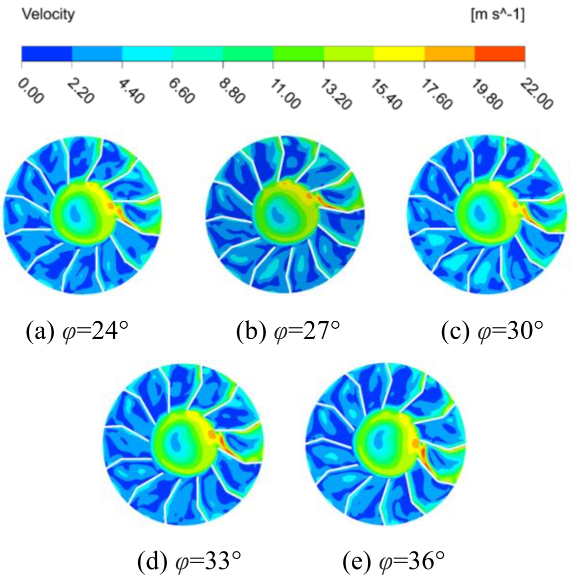

Fig. 21 Cross section of velocity distribution at 0.6Q_d

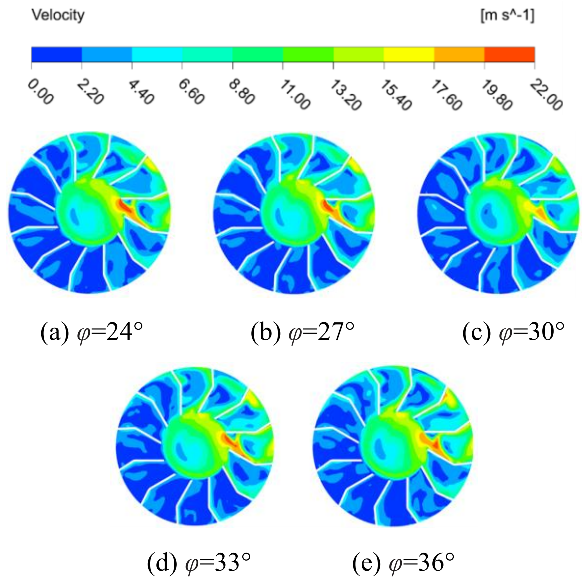

Fig. 22 Cross section of velocity distribution at 1.0Q_d

6. CONCLUSION

Under the same condition of e, the highest efficiency operating point appears at 0.8 Q_d. The cyclone pump head rises and then falls as the flow rate increases. Increasing the vane thickness narrows the flow channel, and under the flow rate of 1.0 Q_d, a vortex is induced in the outlet of the impeller when the fluid is discharged. Efficiency changes slightly with vane thickness adjustments. With the flow increase from 0.6 Q_d to 0.8 Q_d, the efficiency at e = 4.0 mm and e = 4.8 mm rose by 3.60% and 4.90%, respectively. Under the flow rate of 1.2 Q_d, as the vane thickness increased from 3.2 mm to 4.4 mm the efficiency gradually dropped to its lowest value. Additionally, as the vane thickness increases, the low-pressure area in the impeller increases, the pump's interface pressure decreases, and the pressure gradient decreases, all of which affect the pump's stability and efficiency.

When b increases, the volume of the lobeless cavity will be reduced, thus reducing the appearance of circulating flow, which is conducive to obtaining better hydraulic performance of the cyclone pump. The efficiency of cyclone pump may increase with the increasing of flow rate, the efficiency increase is of approximately 6% when b = 52.0mm, and the best performance is at 1.0 Q_d when b = 65.0mm. However, too wide a vane will reduce the efficiency. The pressure increases from the inlet to the outlet and the highest pressure point at high flow rate occurs in the runner region near the impeller outlet. The high-pressure area at the spacer's tongue grows larger as the blade's width increases, while the low-pressure area at the impeller's inlet changes locally.

An appropriate increase in φ can enhance the cyclone pump's performance. During this process, H first rises and then falls as the flow rate increases. At 0.6 Q_d, the head peaks when φ = 33° and is lowest when φ = 30°. As the flow rate increases from 0.6 Q_d to 0.8 Q_d, the heads at five deflection angles increase, with a clear and consistent trend. φ = 33° has the highest efficiency at 1.0 Q_d, and φ = 30° has the highest efficiency at 1.2 Q_d, which is 50.40%. In general, the pressure distributions are consistent. As the outlet deflection angle increases, the worm shell outlet flow becomes more uniform, and the impeller inlet's low-pressure zone slightly expands. The overall speed slightly increases as the deflection angle increases, while the area of low speed decreases.

ACKNOWLEDGEMENTS

This study was supported by the Zhejiang Provincial Natural Science Foundation of China (No. LY22E050015), and the Fundamental Research Funds for the Provincial Universities of Zhejiang (2023YW88).

CONFLICT OF INTEREST

The authors declare that they have no known competing financial interests or personal relationships that could have appeared to influence the work reported in this paper.

AUTHORS CONTRIBUTION

Jiajun Hong: Writing-Original Draf; **Yuxin Jin:** Data Curation; **Zhangcheng Huang:** Supervision; **Wenting Wang:** Methodology; **Yunqing Gu:** Writing-Review & Editing; **Chengqi Mou:** Software; **Denghao Wu:** Formal analysis; **Zhenxing Wu:** Validation; **Jiegang Mou:** Conceptualization

REFERENCES

Bordeasu, D., Dragan, F., Filip, I., Szeidert, I., & Tirian, G. O. (2024). Estimation of centrifugal pump efficiency at variable frequency for irrigation systems. *Sustainability*, *16*(10), 4134.https://doi.org/10.3390/su16104134

Chao, W. X., Shi, B. L., Ruan, H., & Dong, W. (2022). The cavitation characteristics of high speed centrifugal pumps with different impeller types. *Frontiers in Energy Research*, *10*, 811690. https://doi.org/10.3389/fenrg.2022.811690

Chen, R. W., Zeng, Y. Z., & Liu, X. B. (2015). *Research on Effects of Blade Thickness on the Low-specific-speed Centrifugal Pump Performance.* Machinery, Materials Science and Energy Engineering (ICMMSEE 2015) Proceedings of the 3rd International Conference (pp. 207-214).https://doi.org/10.1142/9789814719391_0026

Fleder, A., & Böhle, M. (2019). A systematical study of the influence of blade number on the performance of a side channel pump. *Journal of Fluids Engineering*, *141*(11), 111109. https://doi.org/10.1115/1.4043166

Gao, X., Zhao, T., Shi, W., Zhang, D., Shi, Y., Zhou, L., & Chang, H. (2020). Numerical investigation of an open-design vortex pump with different blade wrap angles of impeller. *Processes*, *8*(12), 1601. https://doi.org/10.3390/pr8121601

Gu, Y., Ma, L., Yan, M., He, C., Zhang, J., Mou, J., Wu, D., & Ren, Y. (2022). Strategies for improving friction behavior based on carbon nanotube additive materials. *Tribology International*, *176*, 107875. https://doi.org/10.1016/j.triboint.2022.107875

Gu, Y., Qiu, Q., Ren, Y., Ma, L., Ding, H., Hu, C., Wu, D., & Mou, J. (2024). Cavitation flow of hydrofoil surface and turbulence model applicability analysis. *International Journal of Mechanical Sciences*, *277*, 109515.https://doi.org/10.1016/j.ijmecsci.2024.109515

Gu, Y., Yin, Z., Yu, S., He, C., Wang, W., Zhang, J., Wu, D., Mou, J., & Ren, Y. (2023). Suppression of unsteady partial cavitation by a bionic jet. *International Journal of Multiphase Flow*, *164*, 104466. https://doi.org/10.1016/j.ijmultiphaseflow.2023.104466

Li, W. (2022). Vortex Pump as Turbine for Energy Recovery in Viscous Fluid Flows with Reynolds Number Effect. *Journal of Fluids Engineering*, *144*(2), 021207. https://doi.org/10.1115/1.4051313

Liu, Y. F., Zhou, J. X., Guo, Q., Shen, A. L., & Zhang, J. (2021). 3-D CFD simulation of transients in multiple pump system with some pumps being stopped. *Journal of Hydrodynamics*, *33*(3), 583-592.https://doi.org/10.1007/s42241-021-0042-8

Mendoza-Escamilla, V. X., Alonzo-García, A., Mollinedo, H. R., González-Neria, I., Yáñez-Varela, J. A., & Martinez-Delgadillo, S. A. (2018). Assessment of k–ε models using tetrahedral grids to describe the turbulent flow field of a PBT impeller and validation through the PIV technique. *Chinese Journal of Chemical Engineering*, *26*(5), 942-956. https://doi.org/10.1016/j.cjche.2018.02.012

Qiu, Q., Gu, Y., Ma, L., Hu, C., Ding, H., Wu, D., ... & Wu, Z. (2024). Study of non-constant local cavitation suppression in micro-wedge structure. *Physics of Fluids*, *36*(1).https://doi.org/10.1063/5.0191165

Wang, C., Chen, X., Ge, J., Cao, W., Zhang, Q., Zhu, Y., & Chang, H. (2023). Internal flow characteristics of high-specific-speed centrifugal pumps with different number of impeller blades under large flow conditions. *Machines*, *11*(2), 138. https://doi.org/10.3390/machines11020138

Wu, X., Shao, C., Tan, M., Liu, H., Hua, R., & Li, H. (2024). Unsteady flow and excitation characteristics in a vortex pump. *Flow Measurement and Instrumentation*, *100*, 102716. https://doi.org/10.1016/j.flowmeasinst.2024.102716

Xu, Z., Kong, F., Tang, L., Liu, M., Wang, J., & Qiu, N. (2022). Effect of blade thickness on internal flow and performance of a plastic centrifugal pump. *Machines*, *10*(1), 61.https://doi.org/10.3390/machines10010061

Yin, Z., Gu, Y., Fan, T., Li, Z., Wang, W., Wu, D., ... & Zheng, S. (2022). Effect of the inclined part length of an inclined blade on the cavitation characteristics of vortex pumps. *Machines*, *11*(1), 21. https://doi.org/10.3390/machines11010021

Zeng, G., Li, Q., Wu, P., Qian, B., Huang, B., Li, S., & Wu, D. (2020). Investigation of the impact of splitter blades on a low specific speed pump for fluid-induced vibration. *Journal of Mechanical Science and Technology*, *34*, 2883-2893. https://doi.org/10.1007/s12206-020-0620-7

Zhang, Y. L., Zheng, S. H., & Zhao, Y. J. (2024). Numerical investigation of flow characteristics in the front and rear chambers of centrifugal pump and pump as turbine. *Scientific Reports*, *14*(1), 11955.https://doi.org/10.1038/s41598-024-62831-4

Zhao, K., Tan, M., Wu, X., Shao, C., & Liu, H. (2023). Effect of impeller installation position on unsteady flow characteristics of a vortex pump. *Engineering Computations*, *40*(2), 335-347. https://doi.org/10.1108/EC-04-2022-0195